ELSEVIER

Physica D 133 (1999) 49–65

PHYSICA D

www.elsevier.com/locate/physd

The Camassa–Holm equations and turbulence

S. Chen [a,*], C. Foias [a,b], D.D. Holm [a], E. Olson [a,b], E.S. Titi [c,d], S. Wynne [c,d]

[a] *Theoretical Division and Center for Nonlinear Studies, Los Alamos National Laboratory, Los Alamos, NM 87545, USA*

[b] *Department of Mathematics, Indiana University, Bloomington, IN 47405, USA*

[c] *Departments of Mathematics, Mechanical and Aerospace engineering, University of California, Irvine, CA 92697, USA*

[d] *Institute for Geophysics and Planetary Physics, Los Alamos National Laboratory, Los Alamos, NM 87545, USA*

Abstract

In this paper we will survey our results on the Camassa–Holm equations and their relation to turbulence as discussed in S. Chen, C. Foias, D.D. Holm, E. Olson, E.S. Titi, S. Wynne, The Camassa–Holm equations as a closure model for turbulent channel and pipe flow, Phys. Rev. Lett 81 (1998) 5338. S. Chen, C. Foias, D.D. Holm, E. Olson, E.S. Titi, S. Wynne, A connection between the Camassa–Holm equations and turbulent flows in channels and pipes, Phys. Fluids, in press. In particular we will provide a more detailed mathematical treatment of those equations for pipe flows which yield accurate predictions of turbulent flow profiles for very large Reynolds numbers. There are many facts connecting the Camassa–Holm equations to turbulent fluid flows. The dimension of the attractor agrees with the heuristic argument based on the Kolmogorov statistical theory of turbulence. The statistical properties of the energy spectrum agree in numerical simulation with the Kolmogorov power law. Furthermore, comparison of mean flow profiles for turbulent flow in channels and pipes given by experimental and numerical data show acceptable agreement with the profile of the corresponding solution of the Camassa–Holm equations.

Keywords: Camassa–Holm equations; Turbulent channel and pipe flows

1. Introduction

The Camassa–Holm equations are well suited to modeling the statistical properties of turbulent fluid flows. We first recall the method of averaged Lagrangians and the derivation of the Camassa–Holm equations. We then summarize the results on existence, uniqueness, and regularity of solutions to the viscous Camassa–Holm equations and compare these results with the known results for the Navier–Stokes equations. Next, we present the estimate of the attractor and a graph of the energy spectrum that shows the Camassa–Holm equations in a periodic box are consistent with the Kolmogorov theory of isotropic and homogeneous turbulence. In particular, the dimension of the attractor is bounded by $(\ell/\ell_{\mathrm{d}})^3$ where ℓ is a macro-scale and ℓ_{d} is the Kolmogorov dissipation length and the energy spectrum decays with the well known Kolmogorov 5/3 power law. Finally we use the Camassa–Holm equations to model turbulent flows in channels and pipes.

* Corresponding author.

0167-2789/99/$ – see front matter
PII: S0167-2789(99)00098-6

In our previous papers [5,6] the Camassa–Holm equations were also used to model turbulent flows in channels and pipes. Here we present a theory with α constant throughout the width of the channel that has not been discussed before. This theory has the advantage of simplicity and builds intuition on how the method of averaged Lagrangians works in the case of channel and pipe flows. However, this approximate theory applies well only for low to moderate Reynolds numbers. At high Reynolds numbers the mean velocity profiles for this theory show a non-physical bump near the boundaries just outside the viscous regime.

The difficulties with the simplified theory seem to be resolved when we allow α to vary near the boundaries. However, only for pipe flows do the experimentally produced data have Reynolds numbers high enough to exhibit the full need for such a theory. In our previous papers [5,6] for ease of presentation this theory was derived for the geometry of the channel. Then analogous results for the more complicated geometry of the pipe were stated. In this paper we give the calculation specifically for the geometry of the pipe fully illuminating the mathematics behind the theory presented already. Moreover, for completeness we discuss also other theoretical aspects of work on the viscous Camassa–Holm equations.

2. The viscous Camassa–Holm equations

A detailed derivation of the Camassa–Holm equations appears in [6]. Basically, we decompose turbulent Lagrangian trajectories into mean and fluctuating parts, make a first order approximation, and then average in the Lagrangian picture. To obtain a PDE we use the Euler–Poincaré equations

$$\left(\frac{\partial}{\partial t} + (u \cdot \nabla)\right) \frac{1}{D}\frac{\delta L}{\delta u} + \frac{1}{D}\frac{\delta L}{\delta u_i}\nabla u_i - \nabla \frac{\delta L}{\delta D} = 0 \tag{2.1}$$

for the averaged Lagrangian L as in [13] and then at the end add a viscous term. In such a way we obtain the dissipative Camassa–Holm equations

$$\frac{\partial}{\partial t} v + (u \cdot \nabla)v + v_j \nabla u_j = \nu \Delta v - \nabla \pi, \qquad \operatorname{div} u = 0 \tag{2.2}$$

where

$$v = u - (\nabla \cdot \langle \sigma \rangle)u - \partial_i(\langle \sigma_i \sigma_j \rangle \partial_j u) \tag{2.3}$$

is the momentum per unit of mass. Here, u is the Eulerian velocity field corresponding to the averaged Larangian trajectory, π is a modified pressure, and σ is a random vector which denotes the fluctuating displacement of the actual Lagrangian trajectory from the averaged one. The angular brackets denote averages with respect to the underlying probability distribution of the random fluctuations in the Lagrangian trajectories. Note that our choice of the viscous term is of the form $-\nu\Delta v$ and not $-\nu\Delta u$. The latter case is the case of the second grade non-Newtonian fluid [9,10].

It is interesting to note that the main difference between this approach and the approach used in deriving the Reynolds equations is the order in which the steps are performed. To derive the Reynolds equations one first obtains the Euler equations as the critical points of the Lagrangian, one then adds the viscous term to obtain the Navier–Stokes equations, and finally one takes ensemble averages. Whereas in our approach, we first average over the Lagrangian fluctuation to get an approximate averaged Lagrangian, we then obtain a PDE as the critical points for the averaged Lagrangian, and finally we add a viscous term.

Table 1
Comparison of rigorous mathematical results for the 3d Camassa–Holm equation with the Navier–Stokes equations

Question	VCHE	2DNS	3DNS
a. Existence of global weak solutions	Yes	Yes	Yes
b. Uniqueness of global weak solutions	Yes	Yes	Unknown
c. Existence of local weak solutions	Yes	Yes	Yes
d. Existence of global strong solutions	Yes	Yes	Unknown
e. Existence of global attractor	Yes	Yes	Unknown
f. Physical upper bound for $\dim_f(\mathcal{A})$	Yes	Yes	Unknown

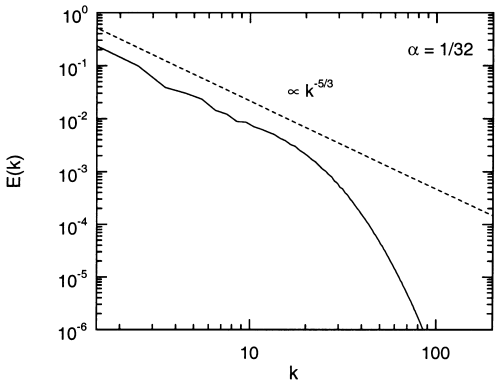

Fig. 1. The energy spectrum of the Camassa–Holm equation in a 3d-box compared with the Kolmogorov 5/3 power law.

3. Space periodic flows

Existence, uniqueness, and regularity of solutions to the Camassa–Holm equations in the period case are studied in [12]. The rigorous mathematical results are comparable among the 3d viscous Camassa–Holm equations (VCHE), the 2d Navier–Stokes (2DNS), and the 3d Navier–Stokes (3DNS). Table 1 summarizes what is known so far. Note that the mathematical theory of the 3d VCHE does not have the pitfalls of the 3DNS equations.

In the case of the Camassa–Holm equations the estimate for $\dim_f(\mathcal{A})$ agrees with the Landau–Lifschitz heuristic argument for number of degrees of freedom for fully developed turbulent flows. In particular [12] the fractal dimension statisfies

$$\dim_f(\mathcal{A}) \le c_0 \left(\frac{\ell}{\alpha}\right)^{3/2} \left(\frac{\ell}{\ell_d}\right)^3 \tag{3.1}$$

where ℓ is a macro-scale, ℓ_d is the analogue of the Kolmogorov's classical dissipation length. The symmetries of the periodic box imply the Lagrangian fluctuations have $\langle\sigma\rangle = 0$ and $\langle\sigma_i\sigma_j\rangle = \alpha^2\delta_{i,j}$. Thus α is a length independent of position related to the statistics of the Lagrangian fluctuations. Scaling arguments for channels and pipes indicate that α is proportional to ℓ. Therefore, the first factor is constant and we obtain exactly the classical estimate.

Recent numerical experiments [4] carried out for $\alpha = 1/32$ show that the energy spectrum of the 3d Camassa–Holm equations is remarkably similar to the accepted theoretical picture for the Navier–Stokes equations. This agreement is demonstrated in Fig. 1.

It is encouraging how well Kolmogorov theory of 3d turbulence agrees with the statistical properties of the viscous Camassa–Holm equations. This is particularly interesting, in light of the fact that the mathematically rigorous results for the viscous Camassa–Holm equations compare more easily with the 2DNS equations. Recall that the 2DNS equations are consistent with the Kraichnan statistical theory of turbulence rather than the 3d Kolmogorov theory. Note that the estimates of $\dim_f(\mathcal{A})$ for the 3d VCHE is consistent with the Kolmogorov theory of 3d turbulence in

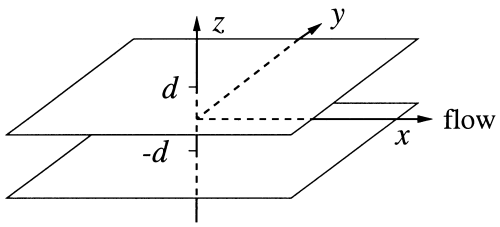

Fig. 2. Choice of coordinates for the infinite channel.

the same way as the dimension of the attractor for the 2DNS equations are consistent with the Kraichnan theory of turbulence [7,11].

4. The channel geometry

We consider fluid flowing between two parallel plates shown in Fig. 2 separated by a distance of $2d$.

4.1. The viscous Camassa–Holm in the channel

The time independent version of Eq. (2.2) is given by

$$(u \cdot \nabla)v + v_j \nabla u_j = \nu \nabla v - \nabla \pi, \qquad \operatorname{div} u = 0 \tag{4.1}$$

where again

$$v = u - (\nabla \cdot \langle \sigma \rangle)u - \partial_i(\langle \sigma_i \sigma_j \rangle \partial_j u) \tag{4.2}$$

is the momentum per unit of mass. Since u represents a mean velocity, solutions to this equation correspond to statistically stationary flows in the x direction. The even symmetry of the mean velocity about the mid-plane of the channel and the translation invariance in the y direction implies that u, which points in the x direction, depends only on z and is even symmetric. Similarly, the ensemble averages of the fluctuations σ only depend on z. Thus we write

$$u = (U(z), 0, 0), \qquad \alpha^2(z) = \langle \sigma_3^2 \rangle, \quad \text{and} \quad \beta(z) = \langle \sigma_3 \rangle$$

and substitute into Eq. (4.1). Noting that

$$\nabla \cdot \langle \sigma \rangle = \beta', \qquad \partial_i(\langle \sigma_i \sigma_j \rangle \partial_j u) = (\alpha^2 U')', \quad \text{and} \quad v = (V(z), 0, 0)$$

we obtain the time-independent viscous Camassa–Holm equations for the channel

$$\nu V'' = \partial_x \pi, \qquad 0 = \partial_y \pi, \quad \text{and} \quad -VU' = \partial_z \pi \tag{4.3}$$

where

$$V = U - \beta' U - (\alpha^2 U')' \tag{4.4}$$

subject to the boundary conditions

$$U(\pm d) = 0 \quad \text{and} \quad \nu U'(\pm d) = \mp \tau_0$$

where τ_0 is the boundary shear stress. We also require that U is symmetric across the channel. Integrating the third equation in Eq. (4.3) gives

$$\pi = f(x, y) + \int V U' \, \mathrm{d}z$$

and so $\partial_x \pi$ does not depend on z. It follows that $\nu V'' = \pi_0'$ is constant.

Now we write the equation in terms of non-dimensional quantities. First, we recall that the mean Reynolds number R and the skin friction Reynolds number R_0 are defined by

$$R = \frac{\bar{U} d}{\nu} \quad \text{and} \quad R_0 = \frac{u_* d}{\nu}$$

where $u_*^2 = \tau_0$, and

$$\bar{u} = \frac{1}{2d} \int_{-d}^{d} U(z) \, \mathrm{d}z$$

is the mean flux across the channel [17]. Then define

$$\phi(\eta) = \frac{U(z)}{u_*} \quad \text{where} \quad \eta = R_0 \frac{z + d}{d}. \tag{4.5}$$

With this rescaling, the boundary conditions are

$$\phi(0) = \phi(2R_0) = 0, \qquad \phi'(0) = 1, \quad \text{and} \quad \phi'(2R_0) = -1.$$

Integrating $\nu V'' = \pi_0'$ gives

$$\frac{R_0^2}{d^2} \frac{\mathrm{d}}{\mathrm{d}\eta} \left(\alpha^2 \frac{\mathrm{d}\phi}{\mathrm{d}\eta} \right) - \left(1 - \frac{R_0}{d} \frac{\mathrm{d}\beta}{\mathrm{d}\eta} \right) \phi = -f_0 - 3 f_1 \left(1 - \frac{\eta}{R_0} \right)^2 \tag{4.6}$$

where f_0 is a constant of integration and $f_1 = -d^2 \pi_0' / (6 u_* \nu)$. Our basic ansatz is that U in the viscous Camassa–Holm equations is the same as the mean velocity U in the Reynolds equations. Recall that the Reynolds equations are obtained by averaging the Navier–Stokes equations [14]. In particular, we write the solution of the Navier–Stokes equations as $(U + u, v, w)$ where U is the mean velocity in the x direction and u, v, and w are the fluctuating Eulerian velocity components in the x, y, and z directions, respectively, and then take ensemble averages of the Navier–Stokes equations to obtain

$$-\nu U'' + \partial_z \langle uw \rangle = \partial_x P, \qquad \partial_z \langle wv \rangle = -\partial_y P, \quad \text{and} \quad \partial_z \langle w^2 \rangle = -\partial_z P$$

where again $-\partial_x P = p_0$ is constant. Integrating the first equation gives

$$-\nu U' + \langle uw \rangle = z p_0 + p_1.$$

The boundary conditions

$$\langle uw \rangle|_{z=\pm d} = 0 \quad \text{and} \quad \nu U'|_{z=\pm d} = \mp \tau_0$$

imply

$$-\langle uw \rangle = -\frac{z \tau_0}{d} - \nu U'(z)$$

Table 2
Values for C, f_0, f_1, and ξ determined from direct numerical simulation for Reynolds numbers $R_0 = 180$ and 395

R_0	$\phi_{\max}$	Ce^{ξ}	f_0	f_1	ξ
180	18	−26.15	18	−1.6	13
395	20	−27.31	20	−2.1	28

or by Eq. (4.5) in terms of the rescaled variables

$$-\frac{\langle uw\rangle}{\tau_0} = 1 - \frac{\eta}{R_0} - \phi'(\eta). \tag{4.7}$$

Consequently, we can solve for the Reynolds shear stress $-\langle uw\rangle/\tau_0$ in terms of our nondimensionalized mean velocity profile ϕ.

4.2. Globally isotropic homogeneous Lagrangian fluctuations

Kolmogorov theory applies to the case of homogeneous isotropic turbulence. In this case, homogeneity implies α does not depend on position and isotropy implies $\beta = 0$. For the periodic box discussed in Section 3 it is obvious, in the absence of physical boundaries, that the fluctuations should be homogeneous and isotropic. In fully developed turbulent channel and pipe flows, there is good reason to suppose the same for most of the flow region, with the possible exception of the boundary layer. To start, it is reasonable to see what insight can be obtained for the channel by taking α constant and $\beta = 0$ throughout the entire channel width. In this case Eq. (4.6) becomes

$$\frac{R_0^2}{d^2}\alpha^2\phi'' - \phi = -f_0 - 3f_1\left(1 - \frac{\eta}{R_0}\right)^2 \tag{4.8}$$

which has a symmetric solution about $\eta = R_0$ given by

$$\phi = C\cosh\left(\xi\left(1 - \frac{\eta}{R_0}\right)\right) + 3f_1\left(1 - \frac{\eta}{R_0}\right)^2 + 6\frac{f_1}{\xi^2} + f_0 \tag{4.9}$$

where we have set $\xi = d/\alpha$ for notational convenience and C is an undetermined constant. We now compare this solution with the numerical simulations of Kim, Moin and Moser [15] and also [16]. The Reynolds number R_0 is given by the simulation. We determine C, f_0 and f_1 from the equations

$$\phi(0) = 0, \qquad \phi'(0) = 1, \quad \text{and} \quad \phi(R_0) = \phi_{\max}$$

where $\phi_{\max}$ is the experimentally determined average centerline velocity of the flow and ξ is treated as a shape parameter used to fit the data. In particular, for comparison with the numerical simulation we use the values from Table 2. Note that the constant C must be small to balance the exponentially large behavior of $\cosh(\xi(1 - \eta/R_0))$ with $\xi \gg 1$ near the wall where $\eta/R_0 \ll 1$.

In Fig. 3 we graph our resulting function ϕ as well as the Reynolds shear stress $-\langle uw\rangle/\tau_0$ along with the data from the direct numerical simulation.

As might be expected there are some difficulties in the agreement of our solution with the direct numerical simulations near the walls of the channel. This is probably due to the fact that the fluctuations are neither homogeneous nor isotropic in this region. However, our solution shows the correct qualitative behavior away from the boundaries. In particular, our solution has an inflection point near $\eta = 10$ and another one farther from the wall whose position is Reynolds number dependent.

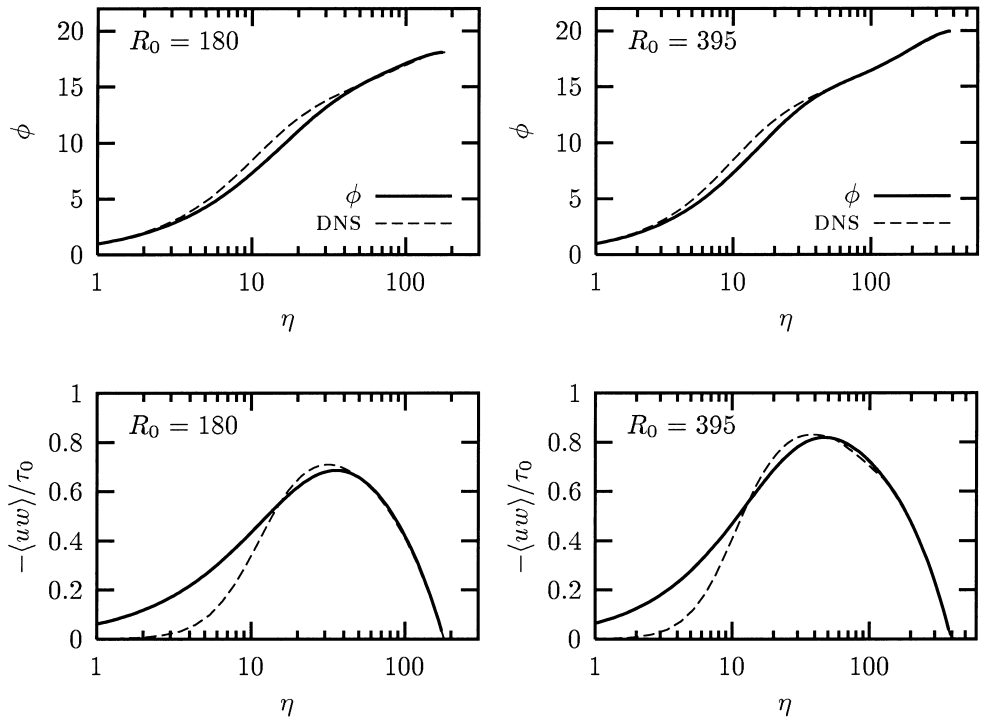

Fig. 3. Comparison of the constant ϕ of the Camassa–Holm equation and the Reynolds shear stress $-\langle uw\rangle/\tau_0$ with direct numerical simulation for turbulent flow in the infinite channel. The solid lines represent our solution while the dashed line represents the numerical simulation of Kim, Moin and Moser [15,16].

We would now like to use this theory to make predictions of the turbulent flow profile as a function of Reynolds number. First note that by writing Eq. (4.9) as

$$\phi = -C\cosh(\xi)\left\{1 - \frac{\cosh(\xi(1-\eta/R_0))}{\cosh(\xi)}\right\} - 3f_1\left\{1 - \left(1 - \frac{\eta}{R_0}\right)^2\right\} \tag{4.10}$$

one realizes the boundary condition $\phi(0) = 0$. For the boundary condition $\phi'(0) = 1$ we differentiate to get

$$\phi' = -\frac{C\xi}{R_0}\left\{\sinh\xi\left(1 - \frac{\eta}{R_0}\right)\right\} - \frac{6f_1}{R_0}\left(1 - \frac{\eta}{R_0}\right).$$

Therefore $\phi'(0) = 1$ becomes

$$-C\xi\sinh(\xi) - 6f_1 = R_0. \tag{4.11}$$

Recall the flux Reynolds number R is defined by

$$R = \frac{\bar{U}d}{\nu} = \int_0^{R_0}\phi\,\mathrm{d}\eta = -CR_0\cosh(\xi)\left(1 - \frac{\tanh\xi}{\xi}\right) - 2R_0f_1. \tag{4.12}$$

Setting $\theta = -6f_1/R_0$ and eliminating C from Eqs. (4.11) and (4.12) gives

$$R_0^2 = \left(R - \frac{\theta R_0^2}{3}\right)\left(\frac{\xi\tanh\xi}{1 - \xi^{-1}\tanh\xi}\right) + \theta R_0^2. \tag{4.13}$$

Upon setting $\xi = \delta R_0$ and taking $\xi \gg 1$, this simplifies to order $O(1/\xi)$ into the basic relation

$$\frac{1-\theta}{\delta} = \frac{R}{R_0} - \frac{\theta R_0}{3}. \tag{4.14}$$

In terms of the parameters θ and ξ, Eq. (4.7) implies the Reynolds shear stress,

$$-\frac{\langle uw\rangle}{\tau_0} = (1-\theta)\left\{1 - \frac{\eta}{R_0} - \frac{\sinh(\xi(1-\eta/R_0))}{\sinh(\xi)}\right\}$$

Thus, $-\langle uw\rangle \geq 0$ for $0 \leq \eta \leq R_0$, as seen empirically. In the lower half of the channel, the solution (4.10) may be expressed to order $O(\xi e^{-\xi})$ as

$$\phi(\eta) = \frac{1-\theta}{\delta}(1 - e^{\delta\eta}) + \theta\eta\left(1 - \frac{\eta}{2R_0}\right), \tag{4.15}$$

for $0 \leq \eta \leq R_0$. In this notation, we have $\alpha = d/\xi = \ell_*/\delta$ for the lengthscale in Eq. (4.8). The velocity profile ϕ in Eq. (4.10) has its maximum at the center of the channel $\eta = R_0$. At this point $\phi_{\max} = \phi(R_0)$ is given to leading order by

$$\phi_{\max} = \frac{1-\theta}{\delta} + \frac{\theta R_0}{2}. \tag{4.16}$$

Recall that the drag coefficient for the channel is defined by $D = 2R_0^2/R^2 = 2u_*^2/\bar{U}^2$. From Eqs. (4.14) and (4.16) we have

$$\theta R_0 = 6\left(\phi_{\max} - \sqrt{\frac{2}{D}}\right), \qquad \frac{1-\theta}{\delta} = 3\sqrt{\frac{2}{D}} - 2\phi_{\max}. \tag{4.17}$$

Since $0 < \theta < 1$, relations (4.17) imply the inequalities $3/2 > \phi_{\max}\sqrt{D/2} > 1$, and we may write

$$\frac{1-\theta}{\delta} = c\sqrt{\frac{2}{D}}, \quad \text{and} \quad \theta R_0 = 3(1-c)\sqrt{\frac{2}{D}}, \tag{4.18}$$

by introducing the constant $c \in (0, 1)$ defined in terms of the velocity profile flatness or centerline velocity ratio $\phi_{\max}/\bar{\phi}$ as

$$\frac{3-c}{2} = \frac{\phi_{\max}}{\bar{\phi}} = \phi_{\max}\sqrt{\frac{D}{2}} \quad \text{with} \quad 0 < c < 1 \tag{4.19}$$

where $\bar{\phi} = R_0^{-1}\int_0^{R_0}\phi(\eta)\,d\eta$. Comparison with the experimental data of Wei and Willmarth [19] shows that c is in the range [0.728, 0.77]. This is consistent with the empirical correlation of $\phi_{\max}/\bar{\phi} = 1.27R^{-0.0116}$ found by Dean [8]. Eq. (4.18)(b) and the basic relation (4.14) then imply

$$\theta = \left(1 + \frac{c\xi}{3(1-c)}\right)^{-1} = O(\xi^{-1}). \tag{4.20}$$

Substituting this into Eq. (4.18)(a) gives

$$R_0 = c\delta R\left(1 + \frac{3(1-c)}{c\xi}\right) = c\delta R + O(\xi^{-1}). \tag{4.21}$$

Thus, to leading order, $\delta = c^{-1}R_0/R = c^{-1}\sqrt{D/2}$ and the velocity profile Eq. (4.15) is given by

$$\phi(\eta) = \frac{R}{R_0}\left\{c\left(1 - e^{R_0\eta/(cR)}\right) + 3(1-c)\frac{\eta}{R_0}\left(1 - \frac{\eta}{2R_0}\right)\right\}. \tag{4.22}$$

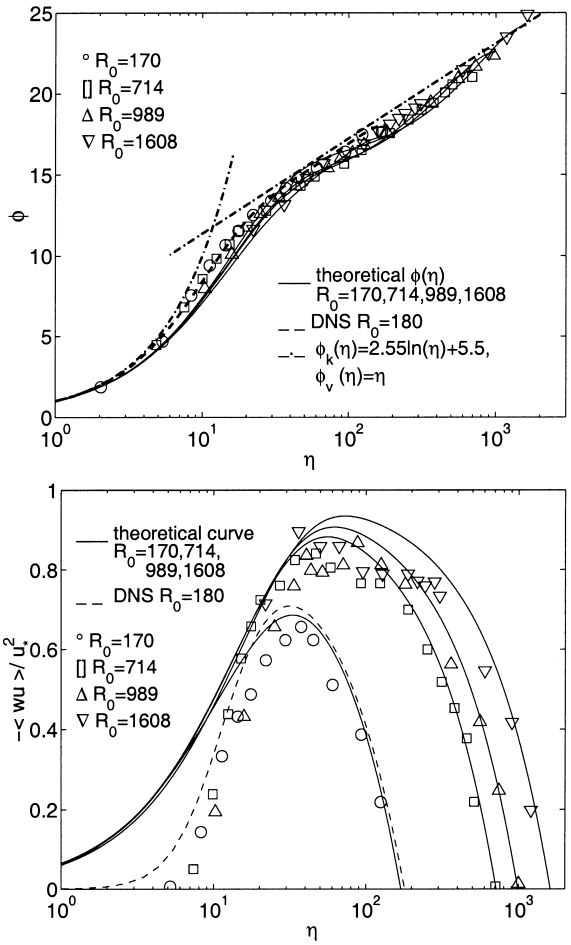

Fig. 4. The mean velocity profiles ϕ and the Reynolds stress $-\langle uw\rangle/\tau_0$ for the constant α version of the Camassa–Holm equations compared with the experimental data of Wei and Willmarth [19] for the channel.

Thus, for $\xi = d/\alpha \gg 1$, the law $\sqrt{D/2} = R_0/R$ and the constant c determine the steady velocity profile of the VCHE $\phi(\eta)$ at each R.

We now introduce one more equation, a drag law. This reduces the number of free parameters so that we can determine our velocity profile ϕ and Reynolds shear stress $-\langle uw\rangle/\tau_0$ solely in terms of the flux Reynolds number. The lengthscale α is given to leading order by $\alpha/d = 1/(\delta R_0) = 2c/(DR)$. For instance, using the Blasius drag law, $D = \lambda R^{-1/4}$ with $\lambda \simeq 0.06$ (see Dean [8]), we obtain

$$\frac{1}{\xi} = \frac{\alpha}{d} = \frac{2c}{\lambda} R^{-3/4} = c\left(\frac{2}{\lambda}\right)^{4/7} R_0^{-6/7}, \quad \text{and} \quad R_0 = \sqrt{\frac{\lambda}{2}} R^{7/8}. \tag{4.23}$$

After the Blasius drag law is chosen and c is determined from the midplane velocity data, no free parameters remain in the model. In Fig. 4 we compare our model to the data of Wei and Willmarth [19].

Also, in Fig. 5 we plot a family of velocity profiles $\phi(\eta; R)$ at various values of R going beyond the values in experimental data in Fig. 4 using the Blasius drag law to determine the extra free parameter. As mentioned earlier the constant C is very small to balance the exponentially large behavior of $\cosh(\xi(1-\eta/R_0))$ near the wall. However,

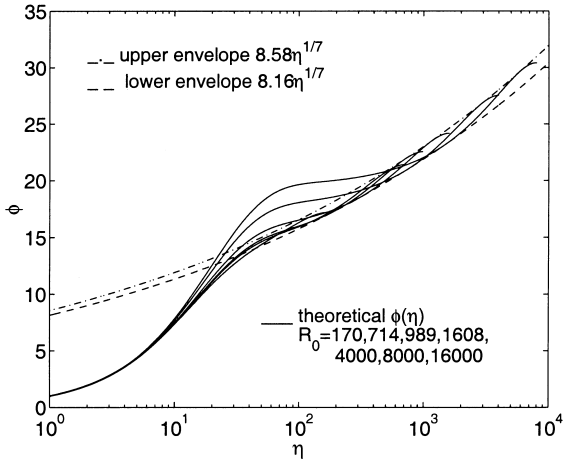

Fig. 5. The upper and lower envelopes of the velocity profile using the Blasius drag law as an input to determine the extra free parameter.

away from the wall this implies that $C\cosh(\xi(1-\eta/R_0)) \approx 0$. As the point of contact of $\phi(\eta; R)$ with its envelope is some distance from the wall, we shall make this approximation in finding the envelopes. In this way, the upper and lower envelopes of this family are found analytically to be $\eta^{1/7}$ power laws up to leading order.

It is interesting to note that Blasius obtains a mean velocity profiles behaving as $\eta^{1/7}$ in the median range of the flow [17]. We get the same functional dependence for the envelopes of the mean velocity profiles as the Reynolds number is varied. Hence, there is a fixed range inside the channel in which our profiles are estimated by the 1/7 power law.

4.3. Locally isotropic homogeneous Lagrangian fluctuations

The results for α constant throughout the channel show some agreement with the numerical and empirical data for moderate skin friction Reynolds numbers $170 < R_0 < 1608$. However, for much larger R_0 Fig. 5 shows that the assumption α constant through the channel leads to a shoulder or overdetermination of ϕ for η around 100. This leads to the physically more reasonable assumption that α, the averaged size of the Lagrangian fluctuations, depends on the distance to the wall in the boundary layer. In this case we still can assume α is constant for most of the flow region but allow it to vary near the wall where β may as well not be zero.

We imagine the Lagrangian fluctuations in the turbulent flow coming from a parameterized family P_z of probability determinations. In this way α and β are given by

$$\alpha^2(z) = \langle\sigma_3^2\rangle = \int_{-d}^{d} (\zeta - z)^2 \,\mathrm{d}P_z(\zeta) \quad \text{and} \quad \beta(z) = \langle\sigma_3\rangle = \int_{-d}^{d} (\zeta - z)\,\mathrm{d}P_z(\zeta). \tag{4.24}$$

This constrains how α and β are related. The Cauchy–Schwarz inequality implies $\beta^2 \leq \alpha^2$. In addition, we note that no fluctuation physically leaves the channel. Thus, the support of P_z must be contained in $[-d, d]$. Therefore in Section 4.3 we assumed the turbulence to be isotropic and homogeneous away from the boundaries. Isotropy implies P_z is symmetric about its mean. Homogeneity implies P_z is a translate $\mathrm{d}P_z(\zeta) = \mathrm{d}P(\zeta - z)$ where P is some fixed distribution. It is reasonable to further assume p_z is unimodal. That is, it has a density with only one peak.

We now pose the question: in the best case, how close to a boundary could these assumptions hold? Let h be the distance from the wall where they break down. The density of the probability distribution must be supported

Table 3
Values for C, f_0, f_1, and ξ determined from direct numerical simulation for Reynolds numbers $R_0 = 180$ and 395

R_0	$\phi_{\max}$	Ce^{ξ}	f_0	f_1	ξ
180	18	−29.40	18	−1.8	20
395	20	−23.47	20	−2.1	32

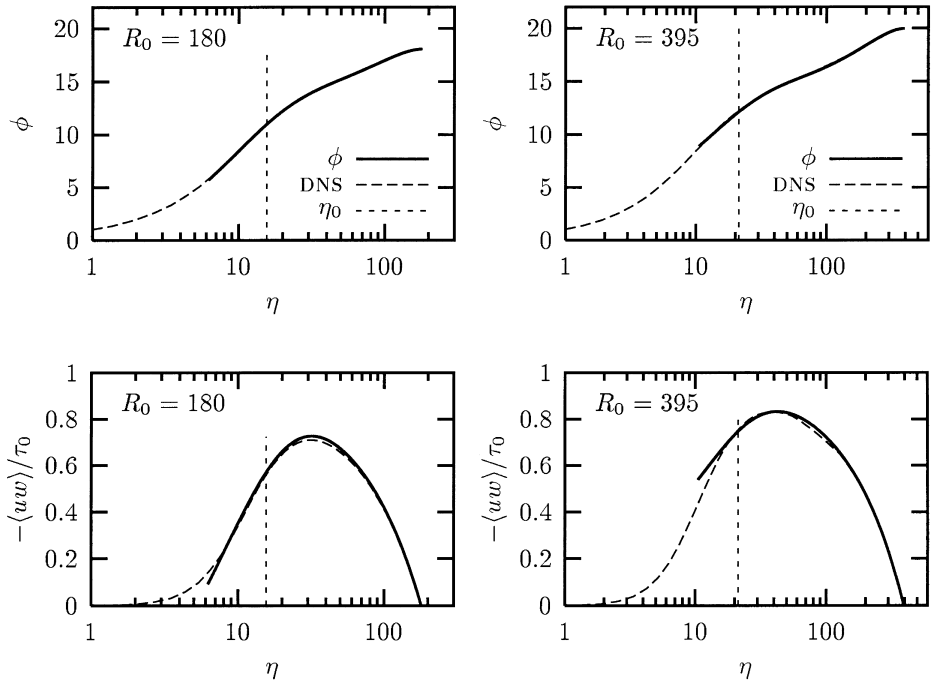

Fig. 6. Comparison of the constant α solution ϕ of the Camassa–Holm equations and the Reynolds shear stress $-\langle uw\rangle/\tau_0$ with direct numerical simulation in the flow region for the infinite channel away from boundaries. The dashed vertical line has been placed at a distance $\eta_0 = \sqrt{3}\alpha$ from the wall to indicate where the assumptions of isotropy and homogeneity are likely to break down.

completely inside the channel. Assuming a density with only one peak, a uniform distribution has the smallest support for a given variance; therefore it is the one which could be translated closest to a boundary. Since

$$\alpha^2 = \frac{1}{2h}\int_{-h}^{h} \zeta^2 \,\mathrm{d}\zeta = \frac{1}{3}h^2 \quad \text{for} \quad |z| \le d - h$$

one finds that $h = \sqrt{3}\alpha$. In terms of wall units, this distance is $\eta = R_0(d-h)/d$.

Thus, for the part of the flow region away from the boundary ϕ takes on the same form as in Eq. (4.9). However, as this solution does not extend all the way to the wall, the boundary condition $\phi(0) = 0$ and $\phi'(0) = 1$ cannot be used to determine free parameters. This gives us additional flexibility in matching the mean flow away from the boundaries.

In Table 3 we choose these parameters so as to obtain a good fit of our profiles and Reynolds shear stresses with the direct numerical simulations away from the viscous sublayer, all the way up to the center of the channel. In Fig. 6 we graph our resulting function ϕ as well as the Reynolds shear stress $-\langle uw\rangle/\tau_0$ along with the data from the direct numerical simulation. Note that the estimate actually serves fine a little below η_0.

The mathematical treatment of the theory of locally isotropic homogeneous Lagrangian fluctuations for high Reynolds numbers appears in our paper [6] along with graphs comparing this theory to the experimental data of Wei

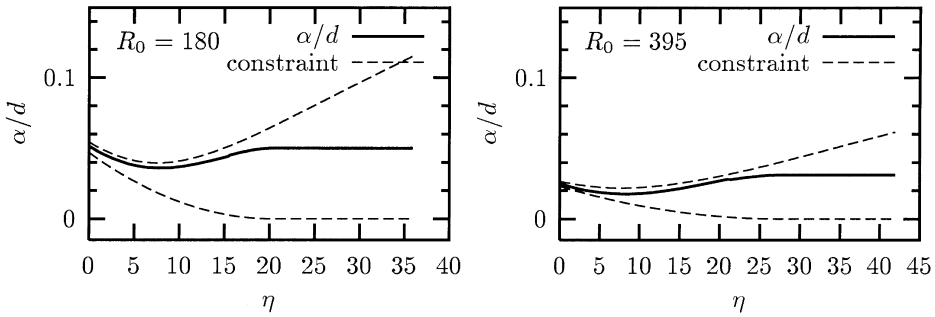

Fig. 7. Statistical compatibility of α and β arising from a uniform probability distribution in the near wall region for ϕ given by direct numerical simulations [15,16]. The lower constraint is given by the Cauchy–Schwarz inequality and the upper constraint by Eq. (4.26).

and Willmarth [19] and Zagarola [20]. In Section 5 we will present this theory for high Reynolds number turbulent flows in pipes.

Before concluding this section let us remark the assumption (4.24), that the statistics of the Lagrangian fluctuations arise from a family of probability distributions, leads to conditions on α and β in the boundary region. In particular, we have Cauchy–Schwarz inequality and the fact that the support of P_z must lie in the channel. The Cauchy–Schwarz inequality implies $\beta^2 \leq \alpha^2$. In [6] the condition that the support of P_z must lie in $[-d, d]$ was given without the further assumption that the underlying probability distributions be unimodal. This leads to the condition that

$$\alpha^2(z) \leq d^2 - z^2 - 2z\beta(z) \quad \text{for} \quad |z| \leq d. \tag{4.25}$$

In this paper, however, we assume that the underlying probability distributions are unimodal. This leads to a more stringent condition than Eq. (4.25) on the relationship between α and β. In fact, we shall show here that it is possible to satisfy the even stronger condition in which the underlying probability distributions are taken to be uniform on their support. Thus, we have that

$$\alpha^2(z) \leq \beta^2(z) + \tfrac{1}{3}(d + z + \beta(z))^2 \quad \text{for} \quad -d \leq z \leq 0. \tag{4.26}$$

Integrating Eq. (4.6) we obtain

$$\frac{R_0^2}{d^2}\alpha^2\phi' + \int_\eta^{R_0}\left(1 - \frac{R_0}{d}\frac{\partial\beta}{\partial\eta}\right)\phi = R_0 f_0\left(1 - \frac{\eta}{R_0}\right) + R_0 f_1\left(1 - \frac{\eta}{R_0}\right)^3. \tag{4.27}$$

From this we solve for α provided that β, f_0, f_1 and ϕ are known. We take ϕ from the direct numerical simulations of Kim, Moin, and Moser [15,16]. The values for f_0 and f_1 have already been determined in Table 3 by matching ϕ in the homogeneous isotropic region away from the boundaries. Finally, to obtain β we take

$$\beta = \begin{cases} \beta_0(1 - \eta/\eta_1)^2 & \text{for } \eta < \eta_1 \\ 0 & \text{for } \eta_1 \leq \eta < R_0 \end{cases}$$

(see Section 14 of [6] for an empirical justification), and choose β_0 and $\eta_1 > \eta_0$ so that α and β satisfy the compatibility condition (4.26) and the Cauchy–Schwarz inequality. The result is shown in Fig. 7. Note that Eq. (4.25) was checked in [6] for higher Reynolds numbers by using the empirical formula from Panton [18] for ϕ near the wall.

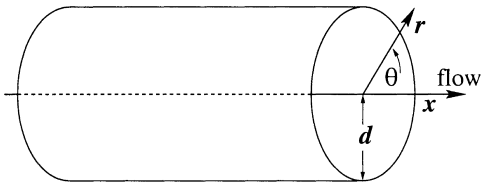

Fig. 8. Choice of coordinates for the pipe.

5. The pipe geometry

In this section we shall develop our method of averaged Lagrangians and Camassa–Holm equations for turbulent fluid through a pipe. We consider a cylindrical pipe shown in Fig. 8 oriented along the x axis of radius d with $y = r\cos\theta$ and $z = r\sin\theta$. Note: we use d for the radius rather than for the diameter of the pipe so as to be consistent with our earlier work where we used d for the channel half height. Also, the Reynolds numbers reported by Zagarola [20] are based on pipe diameter and therefore twice what we use here.

5.1. The Camassa–Holm equations in the pipe

As before we solve the time independent viscous Camassa–Holm equations (4.1). On average the fluid is flowing only in the x direction. Let U be the mean velocity of the fluid in that direction. The symmetry conditions are that U and the averages of the fluctuations σ depend only on r. Therefore we have

$$V\frac{\partial U}{\partial r} = -\frac{\partial \pi}{\partial r}, \qquad 0 = -\frac{1}{r}\frac{\partial \pi}{\partial \theta}, \quad \text{and} \quad -\nu\frac{1}{r}\frac{\partial}{\partial r}\left(r\frac{\partial V}{\partial r}\right) = -\frac{\partial \pi}{\partial x} \tag{5.1}$$

where

$$V = U - \left\{\left(\frac{1}{r} + \frac{\partial}{\partial r}\right)\langle\sigma_r\rangle\right\} U - \left(\frac{1}{r} + \frac{\partial}{\partial r}\right)\left\{\langle\sigma_r^2\rangle\frac{\partial U}{\partial r}\right\} \tag{5.2}$$

Here σ_r denotes the component of σ pointing in the radial direction. The second equation in Eq. (5.1) shows that π is independent of θ. The left side of the last equation of the last equation in Eq. (5.1) only depends on r, hence integrating it with respect to x gives

$$-\pi = -x\frac{\nu}{r}\frac{\partial}{\partial r}\left(r\frac{\partial V}{\partial r}\right) + h(r).$$

Differentiate with respect to r and use the first equation in Eq. (5.1) to obtain

$$-\frac{\partial \pi}{\partial r} = -x\frac{\partial}{\partial r}\left\{\frac{\nu}{r}\frac{\partial}{\partial r}\left(r\frac{\partial V}{\partial r}\right)\right\} + h'(r) = V\frac{\partial U}{\partial r}$$

which is only a function of r. Thus

$$\frac{\partial}{\partial r}\left\{\frac{1}{r}\frac{\partial}{\partial r}\left(r\frac{\partial V}{\partial r}\right)\right\} = 0. \tag{5.3}$$

Solving for the momentum per unit mass V under the assumption that it is bounded at the origin yields

$$V = k_1\left(\frac{r}{d}\right)^2 + k_2 \tag{5.4}$$

where k_1 and k_2 are constants of integration.

5.2. Locally isotropic homogeneous fluctuations

As in Section 4.3 for the channel we suppose the distribution of the Lagrangian fluctuations σ to be isotropic and homogeneous away from the wall of the pipe. In this region we may suppose that

$$\beta = \langle \sigma_r \rangle = 0 \quad \text{and} \quad \alpha^2 = \langle \sigma_r^2 \rangle$$

is independent of r. Therefore Eq. (5.2) simplifies to

$$V = U - \alpha^2 \frac{1}{r} \frac{\partial}{\partial r} \left(r \frac{\partial U}{\partial r} \right).$$

We now express Eq. (5.4) in terms of non-dimensional coordinates ϕ and η (Eq. (4.8)) for the pipe geometry.

$$\frac{R_0^2}{\xi^2} \left(1 - \frac{\eta}{R_0} \right)^{-1} \frac{\partial}{\partial \eta} \left\{ \left(1 - \frac{\eta}{R_0} \right) \frac{\partial \phi}{\partial \eta} \right\} - \phi = -f_0 - 2 f_1 \left(1 - \frac{\eta}{R_0} \right)^2$$

where $f_0 = k_2/u_*$, $f_1 = k_1/(2u_*)$, and $\xi = d/\alpha$. Solving this equation gives

$$\phi(\eta) = C I_0 \left(\xi \left(1 - \frac{\eta}{R_0} \right) \right) + 2 f_1 \left(1 - \frac{\eta}{R_0} \right)^2 + 8 \frac{f_1}{\xi^2} + f_0 \tag{5.5}$$

where

$$I_0(\zeta) = \sum_{n=0}^{\infty} \frac{1}{(n!)^2} \left(\frac{r^2}{4} \right)^n$$

in the modified Bessel function of the first function of the first kind (see, for example [1]). Note that the second term in (5.5) is the classical Hagen–Poiseuille flow for laminar flow in a pipe.

5.3. Prediction of flows in pipes

As before, we make the ansatz that U in the VCHE corresponds to the average velocity in the Reynolds equations. We shall work in terms of the nondimensional mean velocity profiles ϕ. It is accepted, based on experimental data, that ϕ is concave with maximum occurring at the center of the pipe. Hence

$$\left(1 - \frac{\eta}{R_0} \right) \phi(R_0) \le \phi(\eta) \le \phi(R_0). \tag{5.6}$$

Since the flux Reynolds number

$$R = \frac{\mathrm{d}U_{\mathrm{av}}}{\nu} = \frac{2}{d^2} \int_0^d r U(r) \, \mathrm{d}r = 2 \int_0^{R_0} \left(1 - \frac{\eta}{R_0} \right) \phi(\eta) \, \mathrm{d}\eta, \tag{5.7}$$

integrating the inequality (5.6) yields that

$$\frac{\phi(R_0)}{3} \le \frac{R}{R_0} \le \phi(R_0).$$

We also make the empirical observation that

$$\frac{R}{R_0^2} \ll 1 \ll \frac{R}{R_0} \quad \text{for} \quad R_0 \gg 1. \tag{5.8}$$

An in [6] we assume that ϕ has the following scaling property: for R (or R_0) large enough, there exists a range $[q_1, q_2]$ for q in which

$$f(q) = \phi(q_2 R_0) - \phi(q R_0) \tag{5.9}$$

is a function of q only and independent of R_0. We choose q_1 and q_2 so that the assumptions of isotropy and homogeneity hold homogeneity hold in this range; however, we make no assumptions about the size of the range. Note that the classical defect law of Izakson, Millikan and von Mises [17] (pp. 186–188) is the particular case of Eq. (5.9) where $q_2 = 1$ and the range is assumed to be wide. Therefore

$$f(q) = C\{I_0(\xi(1-q)) - I_0(\xi(1-q_2))\} + 2f_1\{(1-q)^2 - (1-q_2)^2\}.$$

Now differentiate to obtain

$$f'(q) = -C\xi I_0'(\xi(1-q)) - 4f_1(1-q) \tag{5.10}$$

$$f''(q) = -C\xi^2 I_0''(\xi(1-q)) + 4f_1 \tag{5.11}$$

$$f'''(q) = -C\xi^3 I_0'''(\xi(1-q)) \tag{5.12}$$

$$f''''(q) = C\xi^4 I_0''''(\xi(1-q)) \tag{5.13}$$

all of which must also be independent of R_0. It follows that

$$-\frac{f''''(q)}{f'''(q)} = \xi \frac{I_0''''(\xi(1-q))}{I_0'''(\xi(1-q))} \tag{5.14}$$

is independent of R_0. Suppose that ξ varies as R_0 varies for large R_0. Then, multiplying by $1-q$ and setting $\zeta = \xi(1-q)$ we would obtain that the quantity

$$\zeta \frac{I_0''''(\zeta)}{I_0'''(\zeta)} = \zeta \frac{\mathrm{d}}{\mathrm{d}\zeta}\{\log(I_0'''(\zeta))\}$$

is independent of ζ in some interval (ζ_1, ζ_2). However, this would imply that on this interval $I_0'''(\zeta) = c\zeta^\gamma$ for some constants c and γ, which is clearly impossible. It follows that ξ must be independent of R_0. Therefore from Eq. (5.12) we have that C is independent of R_0 and from Eq. (5.11) that f_1 is independent of R_0. Hence the only constant that could depend on R_0 is f_0.

Let η_0 be the closest distance to the wall that the statistics of the Lagrangian fluctuations may be assumed isotropic and homogeneous. Thus, the velocity profile found in Eq. (5.5) holds for η in the interval $[\eta_0, R_0]$. From Eq. (5.7) we obtain that

$$\begin{aligned} R = {} & 2\int_0^{\eta_0} \left(1 - \frac{\eta}{R_0}\right) \phi(\eta)\,\mathrm{d}\eta + 2R_0 C \left(1 - \frac{\eta_0}{R_0}\right) \frac{I_0'(\xi(1-\eta_0/R_0))}{\xi} + R_0 f_1 \left(1 - \frac{\eta_0}{R_0}\right)^4 \\ & + R_0 \left(8\frac{f_1}{\xi^2} + f_0\right) \left(1 - \frac{\eta_0}{R_0}\right)^2 \end{aligned} \tag{5.15}$$

from which we can solve for the Reynolds number dependence in f_0 provided the integral can be reasonably approximated. We approximate ϕ on the interval $[0, \eta_0]$ by the piecewise linear function

$$\phi(\eta) \approx \begin{cases} \eta & 0 < \text{for } \eta \le \eta_* \\ \phi(\eta_0) + (n - n_0)\phi'(\eta_0) & \text{for } \eta_* \le \eta \le \eta_0 \end{cases} \tag{5.16}$$

where η_* is chosen so as to make the function continuous. That is, $\eta_* = (\phi(\eta_0) - \eta_0\phi'(\eta_0))/(1 - \phi'(\eta_0))$.

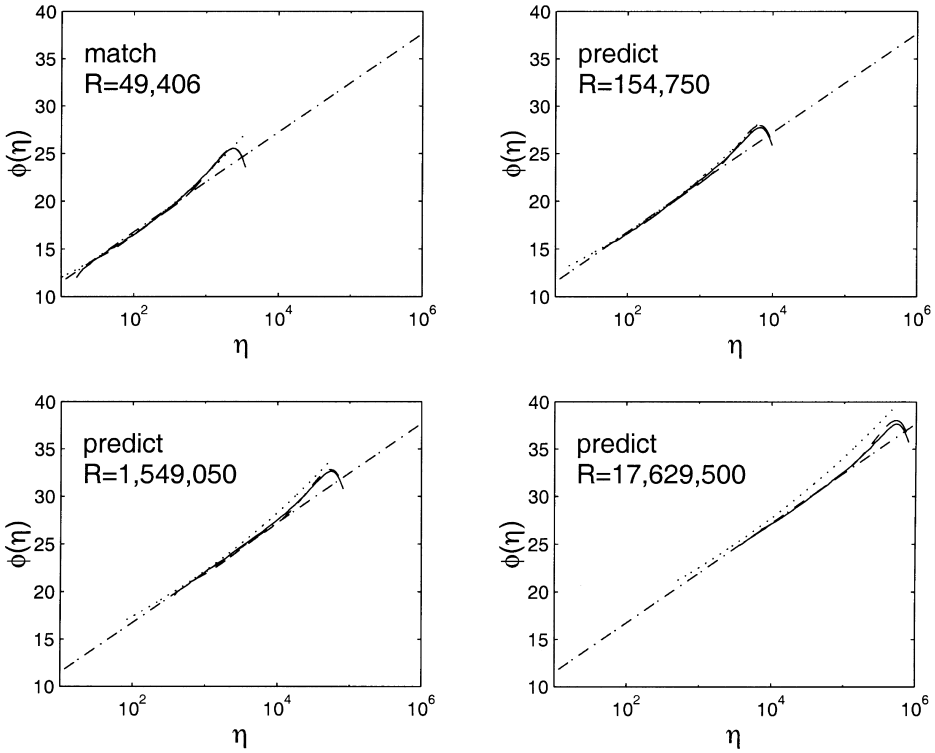

Fig. 9. Prediction of pipe flows. The solid line represents the experimental data from Zagarola [20], the dashed line represents our theoretical profile ϕ, the dash-dotted line represents the von Karman log law, and the dotted line represents the Barenblatt–Chorin–Prostokishin power law [2,3].

Table 4
Given $\xi = 30$, $Ce^{\xi} = -67.81$, and $f_1 = -4.184$ fixed, we predict values of $\phi(\eta_0)$ and f_0 for higher Reynolds numbers

R	R_0	η_0	$\phi(\eta_0)$	f_0
154750	6604	89.92	16.50	27.94
1549050	54721	740.38	21.35	32.80
17629500	525858	7144.94	26.56	38.00

In predicting velocity profiles, there are six free parameters: C, f_0, f_1, ξ, η_0, and R_0. The flux Reynolds number R is given by the experiments. As in the case of channel flow, the parameter R_0 is determined by assuming a drag law and using the relation $R_0^2/R^2 = D/8$. Since C, f_1, and ξ are independent of Reynolds number, we fix these parameters using low Reynolds number experimental data from Zagarola [20]. This is accomplished by choosing two data points in the logarithmic region, and data at the pipe center $\eta = R_0$. This produces a linear system of equations that may be solved for C and f_1. Then, ξ is set, and the two data points chosen as far apart as possible, so that ϕ in Eq. (5.5) best fits the experimental data. We use the first data point $(\eta_1, \phi(\eta_1))$ to set $q_0 = \eta_1/R_0$.

For higher Reynolds numbers, we set $\eta_0 = q_0 R_0$. The parameter f_0 is determined using Eq. (5.15) for R and the approximation (5.16) for ϕ on the interval $[0, \eta_0]$. More specifically, we use Eq. (5.5) with $\eta = \eta_0$ to obtain f_0 in terms of $\phi(\eta_0)$. Using the the cubic term is proportional to $1/R_0$ and is neglected. We solve the remaining quadratic equation for $\phi(\eta_0)$, taking the minimal root which is the one consistent with Eq. (5.8). This in turn gives f_0.

In Fig. 9 we show this predictive capability for ϕ. Each plot graphs the von Karman log-law, the Barenblatt–Chorin–Prostokishin power law [2,3], the Zagarola experimental data [20], and the theoretical curve ϕ for four

different Reynolds numbers. The first post includes the velocity profile for a lower Reynolds number and is used for matching and for setting parameters C, f_1, ξ, and q_0. In particular, we obtain $\xi = 30$, $Ce^{\xi} = -67.81$, $f_1 = -4.184$ and $q_0 = 0.01353$ using such a procedure. The remaining three plots are predicted velocity profiles for higher Reynolds numbers. Table 4 summarizes the values for f_0 used for predicting these flows.

References

[1] M. Abramowitz, I.A. Stegun, Handbook of Mathematical Functions, 9th ed., Dover, New York (1964).
[2] G.I. Barenblatt, A.J. Chorin, Scaling laws and vanishing viscosity limits in turbulence theory, SIAM Rev. 40(2) (1998) 265.
[3] G.I. Barenblatt, A.J. Chorin, V.M. Prostokishin, Scaling laws for fully developed turbulent flow in pipes, Appl. Mech. Rev. 50 (1997) 413.
[4] S. Chen, D.D. Holm, L.G. Margolin, R. Zhang, The 3D DNS of the Camassa–Holm Equations as an LES Model for Turbulence, in preparation.
[5] S. Chen, C. Foias, D.D. Holm, E. Olson, E.S. Titi, S. Wynne, The Camassa–Holm equations as a closure model for turbulent channel and pipe flow, Phys. Rev. Lett. 81 (1998) 5338.
[6] S. Chen, C. Foias, D.D. Holm, E. Olson, E.S. Titi, S. Wynne, A connection between the Camassa–Holm equations and turbulent flows in channels and pipes, Phys. Fluids, in press.
[7] P. Constantin, C. Foias, R. Temam, On the dimension of the attractor in two-dimensional turbulence, Physica D 30 (1988) 284–296.
[8] R.B. Dean, Reynolds number dependence of skin friction and other bulk flow variables in two-dimensional rectangular duct flow, Trans. ASME I; J. Fluids Eng 100 (1978) 215.
[9] J.E. Dunn, R.L. Fosdick, Thermodynamics, stability, and boundedness of fluids of complexity 2 and fluids of second grade, Arch. Rat. Mech. Anal. 56 (1974) 191–252.
[10] J.E. Dunn, K.R. Rajagopal, Fluids of differential type: critical reviews and thermodynamic analysis, Int. J. Eng. Sci. 33 (1995) 689–729.
[11] C. Foias, What do the Navier–Stokes equations tell us about turbulence?, Contemporary Math. 208 (1997) 151–179.
[12] C. Foias, D.D. Holm, E.S. Titi, The Three Dimensional Viscous Camassa–Holm Equations, and Their Relation to the Navier–Stokes Equations and Turbulence Theory, in preparation.
[13] D.D. Holm, J.E. Marsden, T.S. Ratiu, The Euler–Poincaŕe equations and semidirect products with applications to continuum theories, Adv. Math. 137 (1998) 1–81.
[14] J.N. Hunt, Incompressible Fluid Dynamics, Wiley, New York, 1964, p. 127.
[15] J. Kim, P. Moin, R. Moser, Turbulence statistics in fully developed channel flow at low Reynolds number, J. Fluid Mech. 177 (1987) 133–166.
[16] J. Kim, unpublished data from 1989 for $R_0 = 395$.
[17] J.L. Lumley, H. Tennekes, A First Course in Turbulence, MIT Press, Cambridge, MA, 1972.
[18] R.L. Panton, A Reynolds stress function for wall layers, J. Fluids Eng. 119 (1997) 325–329.
[19] T. Wei, W.W. Willmarth, Reynolds-number effects on the structure of a turbulent channel flow, J. Fluid Mech. 204 (1989) 57–95.
[20] M.V. Zagarola, Mean-flow scaling of turbulent pipe flow, PhD Thesis, Princeton University Press, Princeton, NJ, 1996.